Objective Estimation of Tropical Cyclone Wind Structure from Infrared Satellite Data

KIMBERLY J. MUELLER
CIRA/CSU, Fort Collins, Colorado

MARK DEMARIA
NOAA/NESDIS, Fort Collins, Colorado

JOHN KNAFF
CIRA/CSU, Fort Collins, Colorado

JAMES P. KOSSIN
CIMSS/University of Wisconsin—Madison, Madison, Wisconsin

THOMAS H. VONDER HAAR
CIRA/CSU, Fort Collins, Colorado

(Manuscript received 25 March 2005, in final form 28 December 2005)

ABSTRACT

Geostationary infrared (IR) satellite data are used to provide estimates of the symmetric and total low-level wind fields in tropical cyclones, constructed from estimations of an azimuthally averaged radius of maximum wind (RMAX), a symmetric tangential wind speed at a radius of 182 km (V182), a storm motion vector, and the maximum intensity (VMAX). The algorithm is derived using geostationary IR data from 405 cases from 87 tropical systems in the Atlantic and east Pacific Ocean basins during the 1995–2003 hurricane seasons that had corresponding aircraft data available. The algorithm is tested on 50 cases from seven tropical storms and hurricanes during the 2004 season. Aircraft-reconnaissance-measured RMAX and V182 are used as dependent variables in a multiple linear regression technique, and VMAX and the storm motion vector are estimated using conventional methods. Estimates of RMAX and V182 exhibit mean absolute errors (MAEs) of 27.3 km and 6.5 kt, respectively, for the dependent samples. A modified combined Rankine vortex model is used to estimate the one-dimensional symmetric tangential wind field from VMAX, RMAX, and V182. Next, the storm motion vector is added to the symmetric wind to produce estimates of the total wind field. The MAE of the IR total wind retrievals is 10.4 kt, and the variance explained is 53%, when compared with the two-dimensional wind fields from the aircraft data for the independent cases.

1. Introduction

Aircraft reconnaissance is perhaps the best method of estimating hurricane winds. U.S. Air Force Reserve and National Oceanic and Atmospheric Administration (NOAA) aircraft provide in situ measurements of wind, pressure, temperature, and storm position, which are transmitted via satellite to the National Hurricane Center (NHC). Because of cost constraints, most tropical cyclones (TCs) are only flown when they become a threat to U.S. land, and are rarely flown outside of the Atlantic basin. Obviously there is a need for an equally reliable observation platform that is available at all times at all locations.

Without aircraft reconnaissance, forecasters rely more heavily on a method developed by Dvorak (1975, 1984). The goal of Dvorak was to provide estimates of

Corresponding author address: Mark DeMaria, NOAA/NESDIS/ORA, CIRA/CSU, West Laporte Ave., Fort Collins, CO 80523-1375.
E-mail: mark.demaria@noaa.gov

the current and future intensity of TCs, by identifying cloud characteristics from visible and infrared (IR) satellite imagery. While the methods are augmented by a series of empirical rules, pattern interpretations are inherently subjective and can result in varying estimations of intensity.

More recently, Velden et al. (1998) developed an automated method called the objective Dvorak technique (ODT). A computer-based algorithm within the Man-computer Interactive Data Access System (McIDAS) system utilizes several functions to read and analyze Geostationary Operational Environmental Satellite (GOES) IR satellite data to compute an intensity estimate for a targeted TC.

While Dvorak methods provide vital information about TC maximum winds, it is more difficult to estimate a TC's wind structure from IR satellite imagery. At operational forecast centers, TC wind structure is primarily described by such parameters as the radius of maximum wind (RMAX), and the radii of 34-, 50-, and 64-kt winds (1 kt $\approx$ 0.5144 m s^{-1}). These values provide information on how far damaging winds extend from the center of the TC. Because of the high temporal resolution of geostationary satellite data, it would be valuable if these observations could provide information on TC structure via connections between the extent and strength of deep convection, and the extent of damaging winds.

One method for estimating winds from satellites is to track low-level clouds in sequential, high-resolution GOES visible channel imagery (Dunion and Velden 2002). Cloud drift winds provide coverage in the outer radii of the hurricane, where conventional observations like those from buoys and ships are sparse. While important for periphery estimations, they provide little to no information about winds near the eye of the hurricane, because cirrus tends to block tracers at close radii.

Another source of TC wind information is from satellite measurements in the microwave portion of the electromagnetic spectrum. Since NOAA launched the Advanced Microwave Sounding Unit (AMSU) aboard their polar-orbiting satellite series in May 1998, passive microwave warm-core measurements of TCs have been made. The science behind the measurement is that vertical temperature soundings yield information about the mean sea level pressure and wind fields within a TC through thermodynamic and dynamic constraints (Spencer and Braswell 2001; Brueske and Velden 2003).

Demuth et al. (2004) derived a method for estimating TC wind radii via a statistical procedure utilizing AMSU-derived parameters. While AMSU is capable of providing this information, the instruments aboard NOAA polar-orbiting satellites pass over a given point in the Tropics no more than twice a day. Because of the AMSU data gaps in the Tropics there is a chance a TC will remain unobserved over a 24-h period. A missed pass is detrimental to forecasters, as a rapidly deepening TC will exhibit dramatic changes between passes. Another disadvantage of the microwave instrument is that its horizontal resolution is 48 km at nadir, and closer to 100 km near the limbs. Upper-tropospheric warm anomalies can have scales smaller than 50 km and, thus, are not resolvable by the instrument.

While aircraft reconnaissance, visible, and microwave satellite data provide information about TC wind structure, observations may not be continuously available, temporally or spatially. A major advantage of using IR satellite data to observe TCs is that coverage is continuous over the global Tropics and is, therefore, available where ship, aircraft, and microwave data are not. The aim of this investigation is to extend the use of IR data to estimate a storm's structure.

The outline of this research is as follows. Given digital IR information, and a past and current storm position [including latitude, longitude, and an estimate of the maximum wind (VMAX)], it is hypothesized that an accurate estimate of the low-level wind field can be made. To construct a two-dimensional (2D) wind field from a few input parameters, the wind structure will be highly constrained. A modified Rankine vortex model is used to represent the symmetric tangential wind field. The asymmetric part of the wind field can be estimated via the storm motion, and added to the symmetric part to create the entire 2D wind field. With these assumptions the wind field depends on the three parameters of the Rankine vortex, and the motion vector. One parameter of the Rankine vortex is VMAX, which is assumed to be known. The other two Rankine vortex parameters are estimated statistically from the IR data and other basic storm information such as latitude.

The database used to develop this algorithm is described in section 2. Section 3 describes the IR wind algorithm development, which is evaluated on dependent and independent cases in sections 4 and 5. A no-satellite method that includes only latitude and VMAX input is used as a baseline for performance, and the results from the simpler method are compared with the IR method for the dependent and independent cases.

2. Data sources

a. Aircraft reconnaissance data

NOAA and the U.S. Air Force Reserve at Keesler Air Force Base (AFB) have responsibility for aerial hurricane reconnaissance. The U.S. Air Force Reserve

flies a fleet of WC-130 aircraft along a path known as an alpha pattern and collects a flight-level (5000 or 10 000 ft is customary) observation every 10 s. Starting in the northwest quadrant, the aircraft fly a diagonal route across the storm to the southeast quadrant, 105 n mi on either side of the eye. The aircraft then makes a left turn and heads toward the northeast quadrant where it begins a radial leg that ends in the southwest quadrant. After two passes through the eye (fixes), the winds in all four quadrants have been measured. The plane would typically continue the alpha pattern, making two more fixes before heading home.

The aircraft data for the dependent sample used in this research comes from the U.S. Air Force Reserve reconnaissance archive, and encompasses a large sampling of Atlantic basin TCs (77) during the 1995–2003 seasons, as well as a smaller sampling of eastern Pacific TCs (10) over the same time period, for a total of 87 tropical storms and hurricanes in the dependent dataset. There are seven Atlantic basin tropical storms and hurricanes contained in the independent 2004 validation dataset.

It should be pointed out that operational forecast centers are primarily interested in surface winds. There are a number of methods for reducing the flight-level winds to the surface (Powell et al. 1998). However, in this study we did not reduce the data to the surface to eliminate this additional source of uncertainty. The goal of this study is to first determine how well the flight-level observations can be reproduced from IR satellite imagery. Later applications could include a surface reduction procedure, which should take into account the flight level of the original data used to develop the IR algorithm. Typically, the U.S. Air Force Reserve flies at 5000 ft for tropical storms and 10 000 ft for hurricanes. For the data sample used here, the aircraft data were centered near 5000 ft in about 60% of the cases (most of which were tropical storms) and near 10 000 ft in about 40% of the cases (most of which were hurricanes).

b. Objective analysis of aircraft data

The raw aircraft data cannot be used directly to estimate the 2D wind field because of storm motion during the flight pattern, and because they contain some erroneous values. Therefore, a portion of this study was devoted to the development of a comprehensive aircraft dataset, objectively analyzed and meticulously checked for errors.

The first step in data preparation was to perform a gross error check that removed any raw data points that were in error prior to the analysis being done. Gross errors include wind speed less than zero, wind direction greater than 360°, altitude greater than 5000 m, and speed greater than 175 kt.

In preparation for the objective analysis, the lifetime storm files were organized into smaller time periods representative of the wind structure of the system at a given time. The interval chosen must be large enough to encompass a sufficient number of observations, while it must also be small enough that the character of the storm has not changed to such a degree that it is no longer representative of the storm at a given time. The interval chosen was 12 h.

Because a 12-h time interval is used, several flights may have been made during this interval, and several separate center fixes may have been made due to storm motion. For example, in earth-relative coordinates, there were three distinct circulation centers in the measured wind field of TC Lili in 2002 between 1200 UTC on 2 October and 0000 UTC on 3 October (see Fig. 1). The center location at the time of each individual wind observation was determined using cubic interpolation of the 6-hourly best-track data, and the distance east and north of center was adjusted to the best-track center at the end of the 12-h interval. An example of storm-relative winds is shown for Lili in Fig. 1. The storm-relative analysis procedure is similar to that used by the Hurricane Research Division H*wind analysis (Powell et al. 1998). The final step in data preparation was to convert winds from an x- and y-coordinate system to a radial and azimuthal coordinate system, where tangential and radial components of the wind were calculated.

Sufficient data must be available to perform the objective analysis. If there was a data gap of more than 180° in azimuth and 16 km in radius anywhere in the analysis domain (2–202-km radius), then there was insufficient data to proceed. This frequently occurred when only one flight leg was available during a 12-h interval, or when the storm was partially over land.

The next step is to perform a preliminary objective wind analysis. The objective analysis is based upon the model-fitting approach with smoothness constraints described by Thacker (1988). In this approach, the difference between the data and the model counterpart of the data is minimized, where the model is simply the wind components on an evenly spaced grid. The model counterpart of the observations is a bilinear interpolation of the wind components. The smoothness constraints help to fill in the data-void areas of the analysis domain.

As an example, suppose there are K observations of a wind component u, denoted by u_k, at arbitrary locations within a domain $x \in [0, L_x]$, $y \in [0, L_y]$. For the objective analysis, the values of u on an evenly spaced x, y grid with grid spacings of Δx, Δy (denoted by U_{ij})

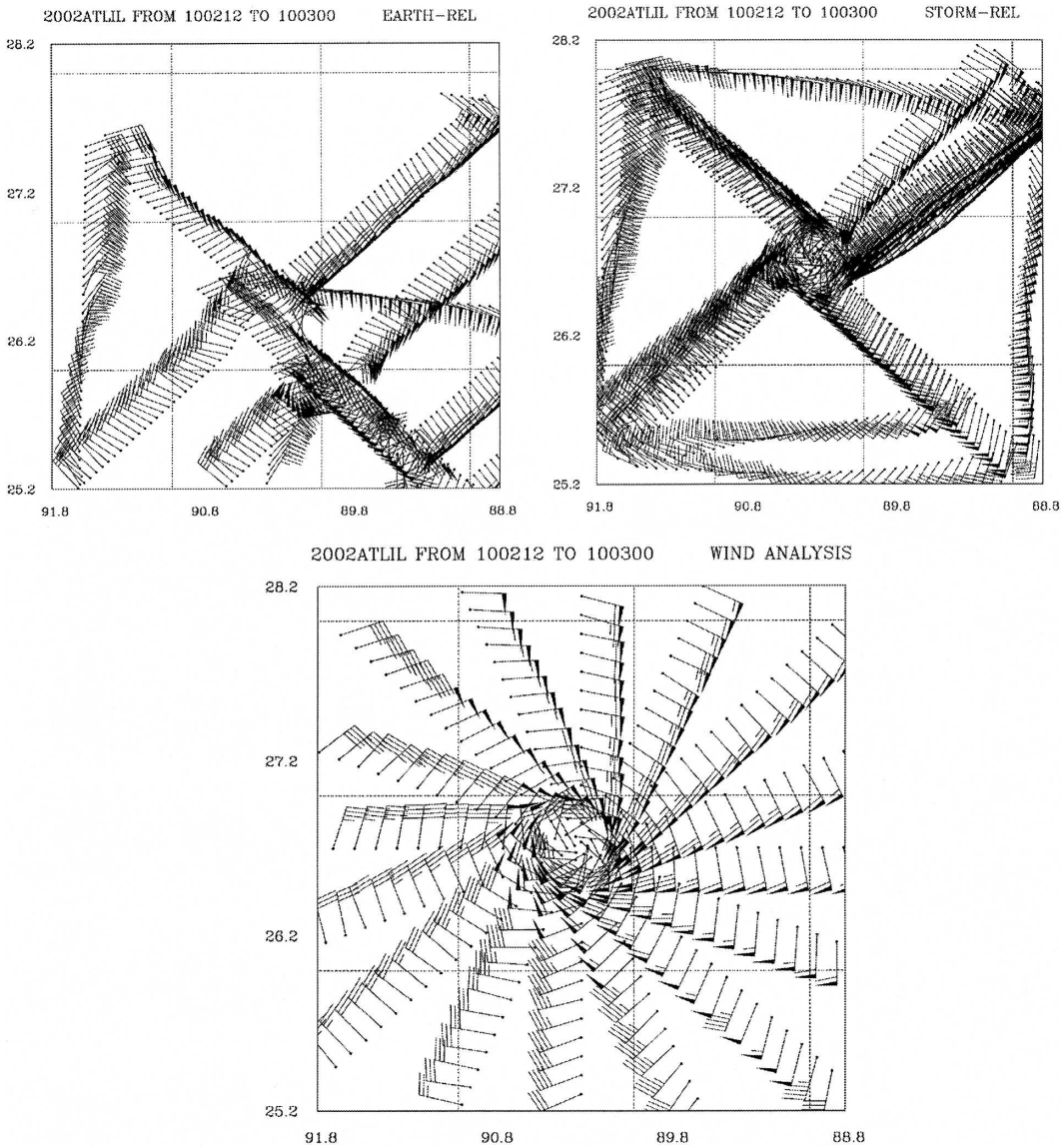

FIG. 1. Hurricane Lili (top left) earth-relative and (top right) storm-relative winds as measured by U.S. Air Force Reserve reconnaissance over the 12-h time period from 1200 UTC 2 Oct to 0000 UTC 3 Oct 2002, and (bottom) the objective analysis of the storm-relative winds.

are determined by minimizing the cost function C defined by

$$C = \frac{1}{2}\sum_{k=1}^{K} w_k(u_k - U_k)^2 + \sum_{i=1}^{I}\sum_{j=1}^{J}[\alpha(\delta_{xx}U_{ij})^2 + \beta(\delta_{yy}U_{ij})^2], \quad (1)$$

where δ_{xx} is the discretized second derivative operator given by

$$\delta_{xx}U_{ij} = (U_{i+1,j} + U_{i-1,j} - 2U_{ij})/\Delta x^2 \quad (2)$$

and similarly for δ_{yy}. In (1), U_k are the wind values bilinearly interpolated from the analysis grid to the observation point k, w_k are data weights, α and β are smoothness parameters, and I and J are the numbers of analysis points in the x and y directions, respectively. The first term on the right-hand side of (1) measures the misfit between the analysis and the observations and the second term is a constraint that acts as a low-pass filter. As shown by DeMaria and Jones (1993) for the one-dimensional case, the filter response function $F(k)$ for the constraint term in (1) can be written as

$$F(k) = 1/\{1 + 8\alpha[1 - \cos(k\Delta x)]^2\}, \quad (3)$$

where $F(k)$ is the amplitude reduction factor of a pure cosine wave with wavenumber k. Because α is in the denominator in (3), it controls the amount of smoothing. For example, for the $2\Delta x$ wave on the analysis grid ($k = 2\pi/2\Delta x$), the amplitude will be reduced by a factor of $(1 + 32\alpha)^{-1}$. Thus, α and β can be chosen to be consistent with the data coverage relative to the analysis grid spacing. In the analysis code, the field U_{ij} that minimized C is found using a simple steepest descent algorithm, which requires the calculation of the gradient of C with respect to U_{ij}. Given the simple form of (1), the gradient is calculated using an analytic formula.

For the aircraft data, the objective analysis is formulated in cylindrical coordinates with 51 radial points ($\Delta r = 4$ km) from $r = 2$ to 202 km and 16 azimuthal points ($\Delta\theta = 22.5°$), and the wind components are input as radial and tangential values. The radial grid points were chosen to match those of the azimuthally averaged GOES data that will be described below in section 2c. An advantage of the cylindrical system is that different smoothness constraints can be applied in the radial and tangential directions. Because the aircraft typically fly an alpha pattern as described previously, the radial and azimuthal spacings of the data are fairly uniform in most cases and the filter functions can be chosen accordingly. For the analysis, α and β were chose so that the half-power wavelengths of the filter were 90 km in radius and 80° in azimuth. All of the data were weighted equally, so $w_k = 1$ in (1).

Aircraft have trouble measuring winds while the aircraft is turning sharply, which happens more often in small storms. However, these errors are not usually large enough to be detected by the gross error checks. Therefore, a method was developed to check for additional bad data by removing observations where the magnitude of the difference between the observed wind vector and that from the preliminary analysis is greater than 75 kt. If the analyzed value is drastically different than the observed value at a given grid point, it indicates that the observed value was very different than the surrounding observed values that contributed to the analysis. If the percentage of bad points in a 12-h interval was greater than 10%, the objective analysis was halted.

After the removal of the bad data, a final objective analysis was performed. An example of an analyzed wind field for the Lili case is shown in Fig. 1, with every fourth radial point plotted. There are 535 wind analyses in the aircraft dataset, composing 94 Atlantic and eastern Pacific storms from the 1995–2004 seasons.

c. CIRA GOES IR archive

The geostationary IR data for this study come from the Cooperative Institute for Research in the Atmosphere (CIRA) tropical cyclone IR (10.7 μm) archive (Zehr 2000). There are normally five geostationary satellites positioned along the equator, giving nearly global coverage. Geostationary satellites have the necessary time resolution and the unique capability of pinpointing the exact locations of intense updrafts by monitoring overshooting cold cloud tops.

The CIRA IR archive includes GOES, *Meteosat*, and Geostationary Meteorological Satellite (GMS) and uses the satellite that provides the best coverage for a particular TC. In this study, all the imagery is from GOES. All digital images are 4-km-resolution Mercator remaps in McIDAS format with 1-byte pixels. The standard time interval between images is 30 min (Zehr 2000). The location of the sector is changed as necessary to keep the center of the TC no more than 4° latitude from the edge of the image. The time period of coverage begins with the first assignment as a tropical depression and ends with the last advisory time.

The objectively analyzed aircraft files were matched to CIRA IR archive files that covered the same 12-h interval of the storm's lifetime. As part of the objective analysis procedure, the actual time of all the data included in the analysis is averaged (the mean analysis time). The mean analysis time provides a measure of when during the 12-h interval the analysis is actually valid. The IR images nearest the mean analysis time are then extracted from the IR archive. Statistical sensitivity tests showed that better fits to the recon analyses were obtained when three IR images were averaged. Thus, in all of the following discussion, the IR input includes the average of the three images closest to the mean analysis time of the recon data. If three images were not available, cases with one or two images were still included in the sample. While there are 535 complete members of the aircraft dataset, the IR matching and maximum wind restrictions (VMAX $>$ 35 kt) brought the dependent dataset to 405 cases, and the validation dataset to 50 cases. If this procedure were applied in real time, the three most recent images could be used. For example, the operational Dvorak estimates use the IR image closest to the synoptic time of interest. For IR winds, the three most recent images before the synoptic time could be used.

Hurricanes Floyd and Iris in Fig. 2 both had maximum sustained winds of 120–125 kt. However, the area coverage of cold clouds in Hurricane Floyd was much larger than that for Iris. This means that convection was occurring on a much broader scale in Hurricane Floyd,

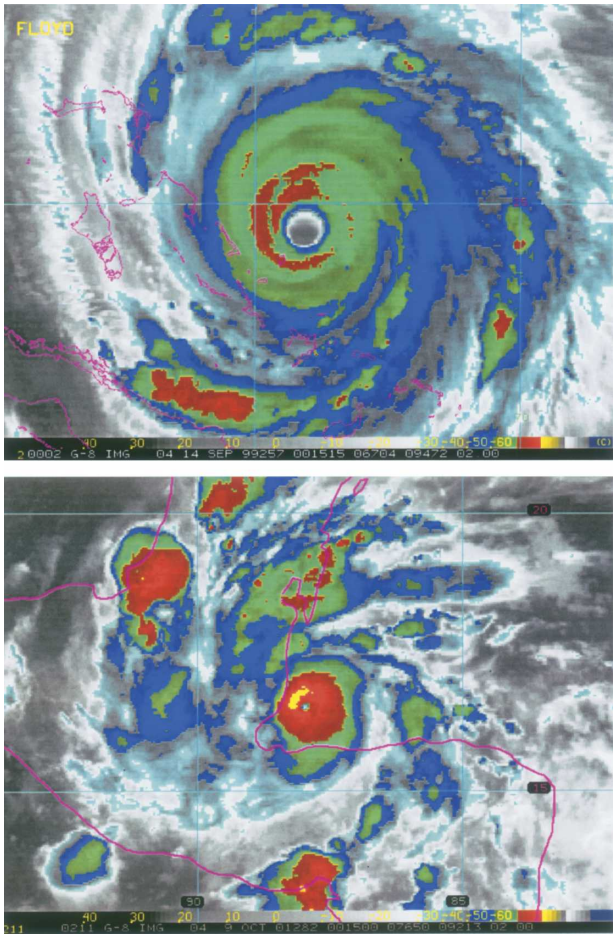

FIG. 2. Color-enhanced GOES IR images of (top) Hurricane Floyd at 1515 UTC 14 Sep 1999 and (bottom) Hurricane Iris at 0015 UTC 9 Oct 2001.

but producing the same intensity as a storm with more confined areas of convection. Importantly, however, the 34-kt wind radii for Floyd were on the order of 190–250 n mi for each quadrant, in contrast to the 60–100 n mi 34-kt wind radii in the much smaller, but equally intense, Iris (see Table 1). This is an illustration of an apparent relationship between cold cloud shield and wind radii. This paper will determine whether quantitative relationships between the geostationary IR parameters and the wind structure parameters from the aircraft data exist.

d. Positions and maximum intensity

As will be described below, the algorithm assumes that the storm position and maximum winds are known. For the both the dependent and independent samples, these were obtained from the NHC working best track, rather than the postseason final best track. The working best track represents the positions and intensity estimates that are available in real time.

TABLE 1. A comparison of the 34-kt wind radii for Hurricanes Floyd and Iris. The wind radii were obtained from the NHC operational forecast/advisory.

Hurricane	Max sustained wind (kt)	R34 (n mi) NE	R34 (n mi) SE	R34 (n mi) SW	R34 (n mi) NW
Floyd	125	250	190	150	190
Iris	120	125	50	40	60

3. Methods

As Holland (1980) suggests, a valid method of using sparse observations to provide objective estimates of wind extent in a TC is with an analytical model of hurricane wind profiles. For the geostationary IR wind algorithm, the symmetric part of the storm circulation is assumed to be represented as the modified Rankine vortex given by

$$V(r) = V_m\left(\frac{r}{R_m}\right) \quad r < R_m,$$
$$V(r) = V_m\left(\frac{R_m}{r}\right)^x \quad r > R_m, \tag{4}$$

where V = tangential wind speed, V_m = maximum tangential wind speed, r = radial coordinate and R_m = radius of maximum wind (referred to as RMAX in the text), and x is a unitless, positive number that determines a storm's size. An important thing to note when using a Rankine vortex is that the entire symmetric wind field is represented by only tangential wind; the radial symmetric wind field is neglected. This assumption is valid according to calculations performed on aircraft data. The symmetric radial wind calculated at each radius is approximately zero (mean of −0.7 kt), and is negligible compared to the symmetric tangential wind at each radius (mean of 40.4 kt). If aircraft were measuring wind speeds near the surface, rather than at the 850- or 700-hPa flight level, the radial wind would have a larger negative component due to friction.

Once the symmetric tangential wind field is constructed, the next step is to consider storm wind asymmetries. For the purpose of this analysis, storm motion was assumed to be the only contributor to TC asymmetry. In reality, there are several factors that cause wind asymmetries, such as horizontal wind shear across the storm domain and convective asymmetries. The storm motion vector was calculated using the working best-track latitude and longitude at the beginning and

end of each 12-h interval in the complementary aircraft wind analyses. A thorough study of the amplitude and phase of the storm motion contribution to the wind asymmetry was performed using aircraft data. The fit of the vortex model to the aircraft data varied from case to case, but in the sample mean, the best fit was obtained by using an asymmetry that was 100% of the storm motion vector, with no phase lead or lag relative to the case where the maximum speed is 90° to the right of the storm motion.

The vortex model described above requires a center position, a motion vector, and the three parameters of the Rankine vortex (R_m, V_m, and x). It will be assumed that the position, motion vector, and maximum winds will be known from other sources (typically from satellite observations in basins without aircraft data and, in our case, from the working best track). The specified maximum wind will include the symmetric and asymmetric parts, so that the maximum wind of the Rankine vortex is given by $V_m = \text{VMAX} - C$, where C is the storm translational speed.

The next step in the analysis is to use the infrared brightness temperature (Tb) to estimate RMAX and x. Instead of estimating x directly, the wind speed near the outer edge of the analysis domain will be estimated (the wind speed at $r = 182$ km, V182), which can then be used to calculate x. Although the analysis domain extended to 202 km, the profiles in the last 20 km appeared noisier (probably due to more limited data coverage), so a radius of 182 was chosen for the indirect estimate of x. A set of possible predictors for RMAX and V182 was derived using the GOES Tb data, as well as storm latitude and VMAX. Because the aircraft data were gathered over a 12-h time period, the best-track intensity at the end of the 12-h period was not necessarily representative of storm intensity at the time in which the majority of the wind measurements were gathered. Therefore, VMAX was estimated by linearly interpolating the working best-track intensity to the average time of the aircraft observations.

The Tb data are reported as a percentage of pixels colder than a particular threshold at each radius from 2 to 202 km, at 4-km intervals. The threshold values are 0°, −10°, . . . , −70°C. An azimuthally averaged Tb is also reported for each radius above. From this information, several relevant predictors were derived. First, a storm total percentage of pixels colder than each of the above thresholds was calculated, and weighted by radius. This yields an overall estimation of the amount of convective activity in the TC. Next, a radius of coldest temperature, as well as a coldest temperature value, were calculated for each storm case.

An alternate method for finding common patterns in datasets was derived through the use of matrix methods from linear algebra. Empirical orthogonal function (EOF) analysis seeks structures that explain the maximum amount of variance in datasets (Hillger and Ellrod 2003). For the purposes of this research, one dimension in the dataset (in this case, the azimuthally averaged Tb as a function of radius) represents characteristic spatial structures that vary with time, which is what we seek, and the sampling dimension is time. The EOF analysis produces a set of structures in the first dimension, called the EOFs, which can be thought of as being the structures in the spatial dimension. The amplitude of the set of structures in the sampling dimension (time) are called the principal components (PCs), and they are related one to one to the EOFs.

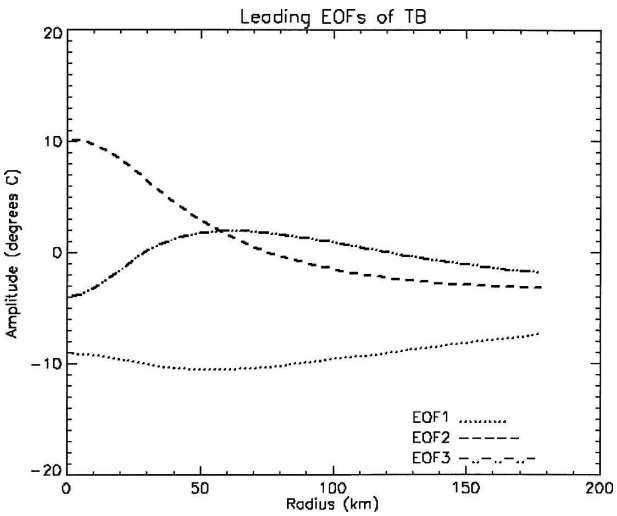

FIG. 3. Leading three EOFs of the IR brightness temperature.

The leading three EOFs of Tb are plotted in Fig. 3. EOF1 of Tb appears to be a manifestation of the mean cold cloud shield. EOF2 likely represents the eye in strong storms, which is warm in the center, surrounded by a cold cloud shield. This EOF is important because it provides information about a storm's size, via the extent of the cold cloud shield. Finally, EOF3 appears to represent a cold Tb maximum near a radius of 55 km, possibly capturing cold cloud tops associated with convection in large eyewalls or spiral bands of the TC. Because the first three EOFs explain 99% of the structural variance in the Tb data, they alone were retained for further analysis.

Although not shown here, the EOFs of aircraft tangential wind fields were also calculated, and are quite similar to the EOFs of Tb, in that EOF1 in both cases picks up the mean radial structure, EOF2 seems to pick up features associated with the eye, and EOF3 illustrates features apparently associated with spiral band-

TABLE 2. Potential predictors of TC RMAX and wind speed at V182.

Potential predictors	Description
SMAX	Azimuthally averaged maximum wind speed from working best track, interpolated to time of average aircraft observation
LAT	Latitude from NHC working best track, for analysis time
PCT00	Storm total percentage of pixels colder than 0°C
PCT 10	Storm total percentage of pixels colder than −10°C
PCT 20	Storm total percentage of pixels colder than −20°C
PCT 30	Storm total percentage of pixels colder than −30°C
PCT 40	Storm total percentage of pixels colder than −40°C
PCT 50	Storm total percentage of pixels colder than −50°C
PCT 60	Storm total percentage of pixels colder than −60°C
PCT 70	Storm total percentage of pixels colder than −70°C
CLDTB	Temperature of azimuthally averaged coldest radius
RDCLD	Radius of coldest azimuthally averaged temperature
CLD52	Azimuthally averaged temperature at $r = 52$ km
CLD102	Azimuthally averaged temperature at $r = 102$ km
CLD152	Azimuthally averaged temperature at $r = 152$ km
CLD182	Azimuthally averaged temperature at $r = 182$ km
SDEV	Storm total standard deviation of brightness temperature
EOFTB1	Leading EOF of brightness temperature, regressed onto Tb profile
EOFTB2	Second-leading EOF of brightness temperature, regressed onto Tb profile
EOFTB3	Third-leading EOF of brightness temperature, regressed onto Tb profile

ing convection. Thus, it is reasonable that the EOFs of Tb can be used to effectively predict structures in the tangential wind field.

Table 2 lists all possible predictors for the RMAX and V182 regressions, described above. All of the parameters are probably relevant to the TC wind structure; however, the actual significance of each one is not explicit. Furthermore, it is not prudent to include every possible predictor in the regression equation, because some may be mutually correlated, providing redundant information. Therefore, the relationship between the predictors and predictands (RMAX and V182 separately) was analyzed with multiple linear regression, using a 1% significance level to select a set of predictors from the list of potential predictors.

4. Dependent results

a. RMAX

The first parameter predicted using multiple linear regression techniques was RMAX. This value is important because it anchors the location of V_m in the Rankine vortex model. There have been relatively few attempts to empirically predict RMAX from infrared satellite data alone.

A regression equation using the natural log of RMAX as the dependent variable, rather than RMAX itself, was derived in an attempt to reduce scatter, especially at smaller RMAX. Thus, LN(RMAX) was predicted for each case, and the exponential subsequently calculated to produce estimates of RMAX. All statistics discussed are based on estimates of RMAX; however, the regression coefficients are based on LN(RMAX) as a dependent variable.

The regression equation for LN(RMAX) retained seven IR-derived predictors, plus SMAX and LAT, explaining 28.8% of the variance in RMAX for the sample of 405 cases. To compare the coefficients for each predictor, normalized coefficients were calculated from nondimensional dependent and independent variables. Table 3 lists the comparable significance of each predictor for LN(RMAX). The normalized coefficients indicate that the most influential predictor was EOFTB1, followed by VMAX. Latitude was of comparable importance to the other IR predictors. The negative coefficient associated with the VMAX predictor suggests that as wind speed increases in a system, RMAX shrinks, as expected physically. The inverse relationship with EOFTB1 is also physically realistic. A Tb profile with colder cloud tops will exhibit a larger positive correlation with PC1, and RMAX will shrink.

Figure 4 is a scatterplot of IR-predicted values versus actual values of RMAX. The regression explains 28.8% of the variance in RMAX, and the MAE is 27.3 km (see Table 4 for all statistical comparisons). The median error is a smaller 16.1 km, indicating that several cases with large errors tend to dominate the mean. Note from the plot that the regression works better for smaller RMAX and tends to underestimate at large RMAX. Not coincidently, a subset of 87 category three hurri-

TABLE 3. Regression variables and their corresponding coefficients, and normalized coefficients used to estimate RMAX and V182.

	RMAX (km) R^2 = 28.8%		V182 (kt) R^2 = 75.0%	
Independent variable	Coefficient	Normalized coefficient	Coefficient	Normalized coefficient
SMAX	−0.008 249 47	−0.366 928	1.071 55	1.773 17
LAT	0.013 875 2	0.150 036	0.744 353	0.299 458
EOFTB1	−0.050 654 8	−0.519 028	5.674 45	2.161 62
CLDTB	−0.000 317 505	−0.011 014 4		
$CLD52^2$	$-3.080\ 12 \times 10^{-5}$	−0.093 799 5		
$CLD102^2$	−0.000 101 828	−0.276 910		
$CLD152^2$	−0.000 112 919	−0.259 006		
CLD52	−0.009 264 47	−0.368 116		
PCT50	0.003 805 14	0.173 606		
EOFTB2			1.071 55	2.745 26
EOFTB3			0.744 353	1.273 99
$SMAX^2$			5.674 45	−1.115 88
CLD182			20.4021	−0.133 511
$CLD182^2$			7.571 13	0.541 551
$CLD152^2$			−0.004 131 94	−0.633 193

cane or greater cases (VMAX > 96.0 kt) performed significantly better than the dataset as a whole, exhibiting a variance explained of 42.1% and a MAE of only 13.8 km. Conversely, a subset of 166 tropical storm strength cases (VMAX < 64.0 kt) represented the poorer performers, exhibiting a variance explained of only 19.7% and an MAE of 36.5 km. However, Fig. 4 also shows that the statistical prediction has difficulty with the smallest storms, and did not produce any RMAX estimates smaller than about 20 km, even though several were observed.

To quantify the improvement over a baseline method, a separate RMAX was predicted by removing all IR-derived predictors in the regression equation described above. This method, which will be called no-sat, produces less significant results. The variance explained using the no-sat method is 18.4%, and the MAE worsens to 32.5 km. Thus, the geostationary IR-predicted RMAX represents a 56.5% improvement in terms of variance explained, and a 19.0% improvement in terms of MAE.

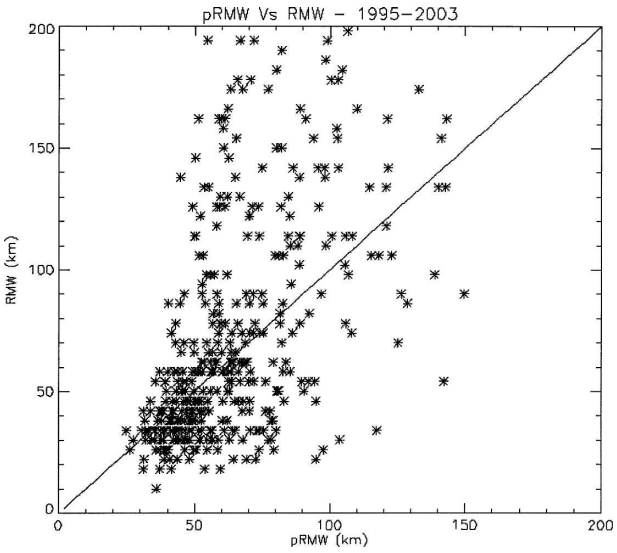

FIG. 4. Scatterplot of IR-predicted RMAX (pRMW) vs aircraft-measured RMAX (RMW).

b. V182

The second parameter predicted using multiple linear regression is V182. This parameter is chosen to represent the storm size and is used to calculate x in the Rankine vortex model.

Six IR-derived predictors are retained in the regression, together with an estimate of SMAX, $SMAX^2$, and LAT, explaining 75.0% of the variance in V182. The MAE for the prediction of V182 is 6.48 kt. A scatterplot of predicted versus actual values of V182 is illustrated in Fig. 5. All of the IR-derived predictors have the effect of strengthening the wind at r = 182 km as the Tb field gets colder. The importance of the relationship between V182 and EOFTB1 physically represents the storm size increasing as the mean cold cloud shield becomes colder. The relationship between V182 and EOFTB2 physically represents that the warmer the eye compared to the surrounding cold cloud shield, the larger the storm size, and consequently the greater the winds at a radius of 182 km. This result is similar to the qualitative relationship between cold cloud area and storm size, illustrated in Fig. 1. Both of these EOF predictors are extremely important in the regression equation, as shown in Table 3.

While the scatterplot suggests impressive results, it is

TABLE 4. Variance explained, MAE, and percent improvement statistics.

		Dependent		Independent	
		R^2 (%)	MAE	R^2	MAE
V182	IR	75.0%	6.48 kt	68.2%	7.98 kt
	No-sat	67.7%	7.41 kt	64.9%	8.46 kt
	Improvement (%)	10.8%	14.4%	5.1%	6.0%
RMAX	IR	28.8%	27.3 km	43.3%	20.0 km
	No-sat	18.4%	32.5 km	18.4%	26.9 km
	Improvement (%)	56.5%	19.0%	135%	34.5%
1D symmetric tangential wind field	IR	78.3%	4.86 kt	79.0%	8.49 kt
	No-sat	72.3%	5.40 kt	76.7%	10.53 kt
	Improvement (%)	8.3%	9.0%	3.0%	24.0%
2D total wind field	IR	43.1%	9.85 kt	53.2%	10.41 kt
	No-sat	36.8%	10.82 kt	46.0%	10.93 kt
	Improvement (%)	17.1%	9.8%	15.7%	5.0%

important to note that the regression equation is also highly dependent on SMAX, as is also shown in Table 3. It is therefore prudent to determine quantitatively the contribution of the IR data to the regression. To do this, the IR-derived V182 estimates were compared to no-sat-derived V182 estimates. A no-sat version of the regression equation produces an R^2 of 67.7%, as compared to the IR-derived R^2 of 75.0%. The MAE for the no-sat-derived V182 degrades from 6.58 to 7.41 kt. A *t*-statistic significance test, with 405 degrees of freedom (representing each independent case), was performed on the case by case MAE for the no-sat versus IR-derived V182 values, to determine if the samples have significantly different means. The results indicate that the difference in the means of the MAE is significant at the 99% level. Thus, the error improvement in the estimate of V182 that occurs as a result of including geostationary IR data is not only quantifiable, but also significant.

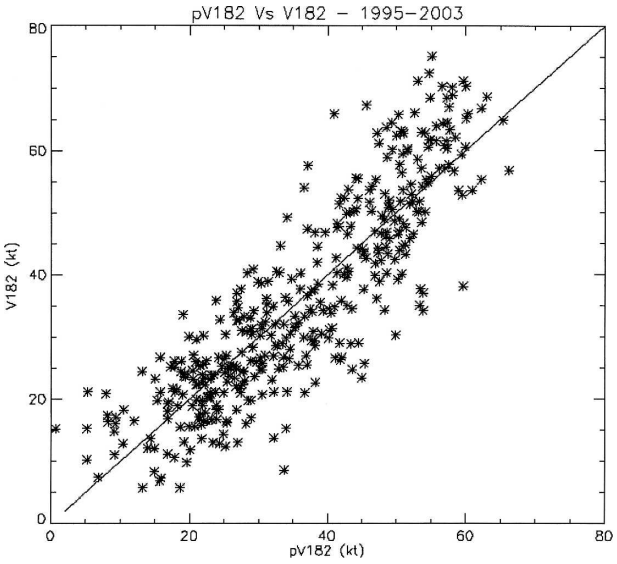

FIG. 5. Scatterplot of IR-predicted V182 (pV182) and aircraft-measured V182 (V182).

c. *Symmetric tangential wind field*

Once estimates of V182 and RMAX are produced from the multiple linear regression techniques, the entire symmetric tangential wind field can be re-created using the Rankine vortex model (described in section 3). See Fig. 6 for an illustration of the geostationary IR constructed wind profiles and their counterpart ground truth aircraft measured wind profiles. Qualitatively, the Rankine vortex model does a sufficient job of reproducing the symmetric wind profile, particularly for hurricane strength cases. It is necessary, however, to quantify the improvement over the no-sat method, and to determine whether the improvement is indeed significant.

The MAE for the no-sat dataset is 5.4 kt, while the MAE for the IR dataset is 4.86 kt; an improvement of 9.0%. Again, the significance of the improvement was determined using a *t* test on the difference in storm total MAE for each of 405 IR-derived wind profiles, and each of their complementary 405 no-sat-derived wind profiles. A *t* test proves significantly different means at the 99.9% level. Therefore, the improvement in the error of the symmetric tangential wind field estimation by adding geostationary IR information is both quantifiable and significant. In addition to improvement in MAE, the variance of the observed symmetric winds explained by the IR-derived symmetric tangential wind profiles is 78.3%, compared to 72.3% explained by the no-sat method alone.

d. *Total wind field*

Finally, once a symmetric tangential wind is estimated, the motion vector is added and the total 2D

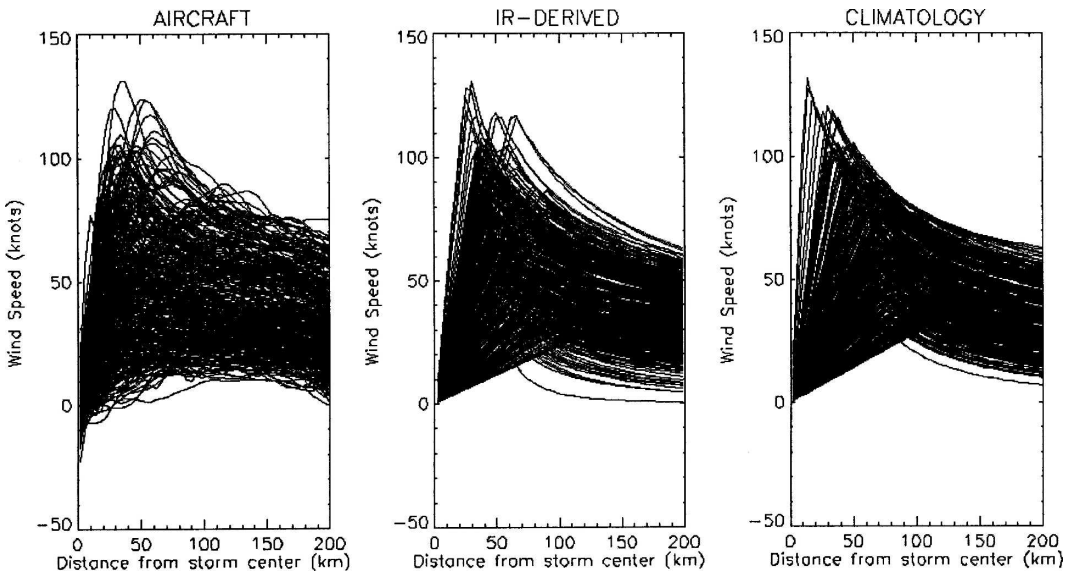

FIG. 6. (left) Aircraft-measured symmetric tangential wind profiles for 405 analysis periods, (middle) their counterpart IR-derived symmetric tangential wind profiles, and (right) their no-sat-derived symmetric tangential wind profiles.

wind field is calculated at all of the points on the aircraft analysis grid (51 radial points and 16 azimuths).

There are two questions to answer after looking at this total derived wind field. First, does the addition of the storm motion vector asymmetry to the IR-derived symmetric wind field more closely approximate the actual aircraft total wind field? Second, does the IR-derived total wind field provide better results than a similar no-sat-based re-creation? Fig. 7 illustrates how the addition of the motion vector affects the wind field. The top two panels represent the aircraft-measured symmetric (right panel) and total (left panel) wind fields. The bottom two panels are the corresponding IR-derived symmetric and total wind fields for Hurricane Hortense on 14 September 1996 at 0000 UTC. The right-hand panels illustrate an IR-derived symmetric wind field that is a slight overestimation of the actual symmetric wind field. Also, the actual symmetric wind field has weak inner and outer wind maximums, while the derived wind field is only capable of resolving one wind maximum, and places it between the two actual maximums. Because the high asymmetry of the storm at this time, the correlation coefficient (CC) between the actual total wind field (Fig. 7, top-left panel) and the derived symmetric wind field (Fig. 7, bottom-right panel) is only 0.273. The lower left-hand panel in Fig. 7 takes into account storm motion, and in fact places the maximum wind 90° to the right of the motion, and now very closely approximates the actual wind field. Given that the algorithm is not capable of resolving the inner and outer wind maximums that were present at the time, the orientation and extent of the high winds is quite accurate once a motion vector derived asymmetry is incorporated. The CC between the actual and derived total wind fields improves dramatically in this case, to 0.788. Of course, this is only one example, of 405 cases, and due to the highly asymmetric nature of the system, the improvement from adding storm motion is going to be more dramatic for Hortense than for more symmetric cases.

To examine the improvement in the entire dataset, Fig. 8 shows a histogram of the CC for the IR-derived symmetric wind field (light gray), the no-sat total wind field (gray), and the IR-derived total wind field (black). There is a definite qualitative improvement due to the addition of a motion vector. At lower bins (at and below 0.4–0.5), the frequency of occurrence of the IR-derived symmetric wind field CC is much higher than the IR-derived total wind field CC. However, above a CC bin of 0.4–0.5, the IR-derived total wind field occurrence is far more frequent. In fact, the mean IR-derived total wind field CC for the 405-case dataset is 0.656 (the IR-derived total wind field explains 43.1% of the variance in the total wind field), while the IR-derived symmetric wind field exhibits a mean CC of 0.509, or an R^2 of 26%. This improvement in CC, which occurs as a result of incorporating storm motion, thus proves the method successful.

Additionally, compared to a baseline no-sat method, the geostationary IR-derived total wind field performs significantly better. Again, refer to Fig. 8 for a histogram of CC. The middle bars, gray in color, represent

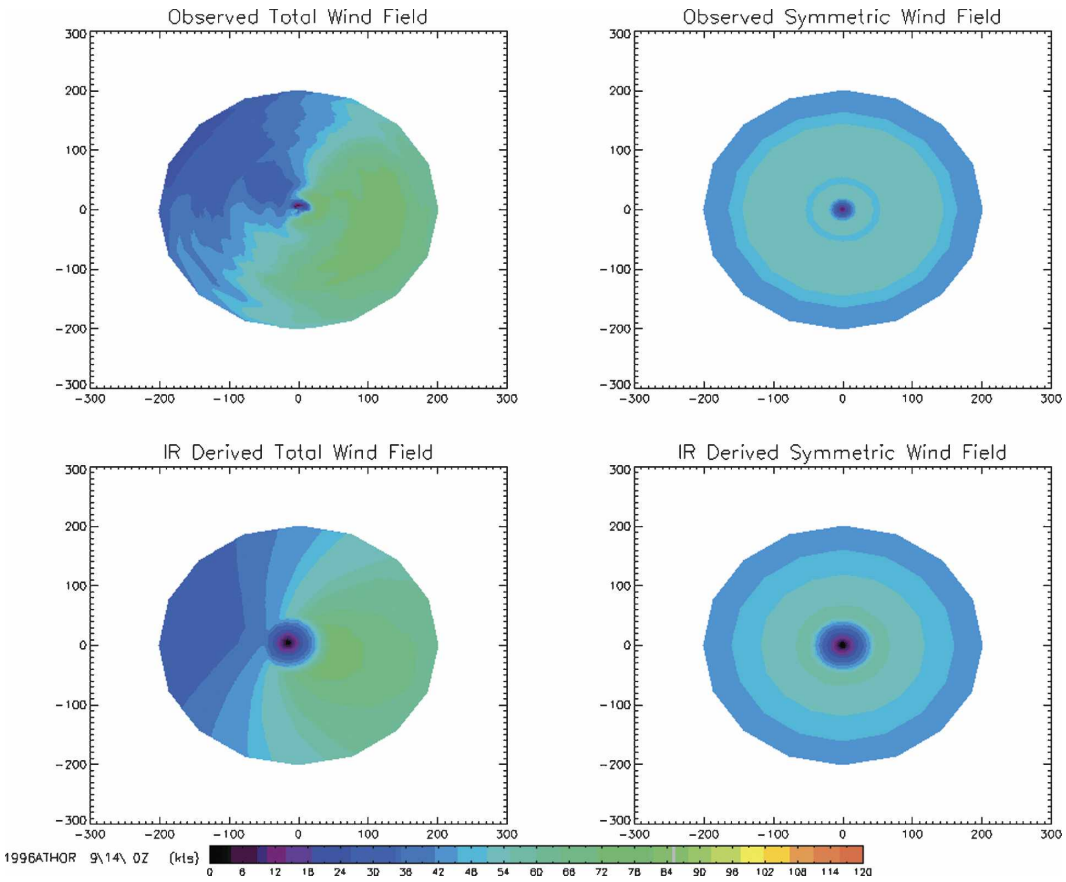

FIG. 7. Four-panel plot of the aircraft-observed vs IR-derived symmetric and total wind fields for Hurricane Hortense at 0000 UTC 14 Sep 1996.

the frequency of occurrence of the no-sat-derived versus aircraft total wind field CC. There is an obvious shift toward lower CC compared to the black bars representing the IR-derived versus aircraft total wind field CC. In fact, only 17 of the no-sat-derived cases are correlated at or higher than 0.90, compared to 32 of the IR-derived cases. The mean CC for the no-sat cases is 0.606, while it improves to 0.656 when the IR information is added to produce a total wind field, an improvement of 8.3%.

An alternate method of quantifying the improvement is to look at the improvement in MAE. An MAE was determined by calculating the difference between IR-derived total wind speed and the aircraft-measured total wind speed at each grid point, and averaged by case. Notice in Fig. 9 the shift toward higher MAE in the no-sat dataset compared to the IR dataset. The average MAE is 9.85 kt for the IR-derived wind field, and 10.82 kt for the no-sat-derived wind field. This is an improvement of 1.0 kt, or 9.8%. A *t* test was performed and the difference in means is significant at the 99.9% level. Refer to Table 4 for a summary of statistics.

5. Independent results

To evaluate further the geostationary IR wind field estimation, the algorithm developed from the 1995–2003 cases was run on 50 cases from the 2004 hurricane season, and results were compared to aircraft-measured winds. In these cases, the working best-track interpolated intensities were used to estimate VMAX, and the 2004 real-time aircraft data have a temporal resolution of only 30 s (compared with 10-s resolution for the postprocessed aircraft data developmental dataset). Because the algorithm is run on cases that were not members of the developmental dataset, the results are indicative of what can be expected when this algorithm is implemented in real time.

a. Statistical comparison

As shown in Table 4, the algorithm is robust, with only a slight increase in error relative to the developmental dataset in most cases, and even a slight decrease in error in estimating RMAX. The algorithm explains 43.3% of the variance in RMAX, compared to a devel-

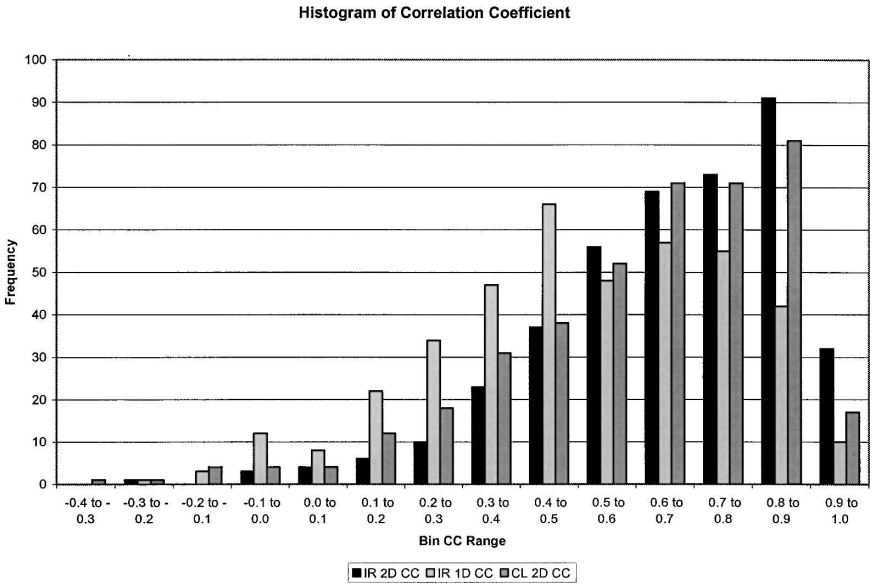

FIG. 8. Histogram of correlation coefficient for 405 no-sat-derived total wind field cases (gray), 405 IR-derived total wind field cases (black), and 405 IR-derived symmetric tangential with field cases (light gray), vs aircraft total wind field.

opmental dataset variance explained of 28.8%. Furthermore, the MAE is 20.0 km for estimating RMAX. The improvements over the no-sat independent estimates are well within the range of the developmental dataset. See Table 4 for statistics.

The hypothesized reason for the improved results is that the 2004 sample has a disproportionately high percentage of category three or greater cases. In fact, 23 of 50 cases exhibit a VMAX of 96.0 kt or greater. As was noted in the previous section, the RMAX algorithm performed better for the >96.0 kt cases in the developmental dataset. Thus, it is not surprising to see robust results in the independent dataset.

The algorithms explain 68.2% of the variance in V182, and the MAE in V182 for the independent cases is 7.98 kt. This is only slightly less robust than the de-

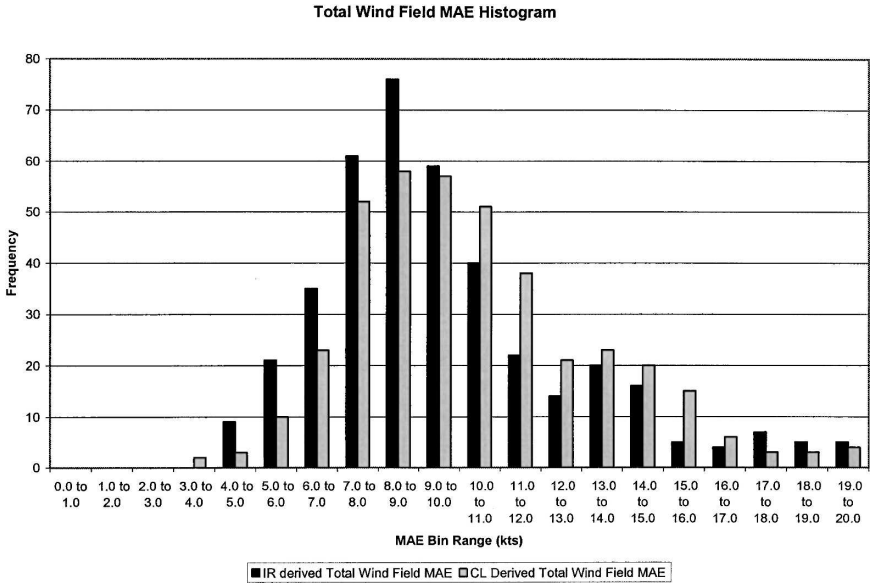

FIG. 9. Histogram of MAE by case for the no-sat-derived total wind field (gray) and the IR-derived total wind field (black), compared with aircraft measurements.

velopmental dataset. Again, improvements over the no-sat method alone are on the order of 6.0% in terms of both error and variance explained.

The Rankine vortex model is utilized to reconstruct the symmetric tangential wind field for each of the 50 independent cases, resulting in an R^2 value of 79.0%, again an improvement over the developmental dataset, and an MAE of 8.49 kt. The increase in MAE error is likely a result of the high wind speeds present in the majority of the 2004 cases. The mean VMAX for the 2004 cases is 90 kt, compared to a mean VMAX of only 72 kt for the developmental cases; thus, errors are bound to be larger. This does not necessarily mean the algorithm is less robust. In fact, the independent error represents 9.4% of the average VMAX, an only slighter larger ratio than the 6.8% for the dependent dataset.

Finally, the addition of a motion vector results in a total wind field variance explained of 53.2%, and an MAE of 10.41 kt. Again, taking into account the greater average strength of the 2004 cases, the slightly larger MAE is not highly significant. It seems likely that the variance-explained increase from 46.1% for the developmental dataset to 54.0% for the independent dataset is partly due to the greater overall intensity of the 2004 cases, since more intense storms tend to have a more predictable structure. In fact, if only VMAX $>$ 96.0 kt systems are considered for the dependent dataset, the total wind field variance explained improves to 56.8%. It is thus clear that stronger systems tend to have a more predictable RMAX using this method and are better represented by the Rankine vortex model and, thus, are better estimated.

For the independent cases, the no-sat method alone explains 46.0% of the variance in the total wind field (compared to 53.2% with the addition of IR predictors). Of note, this 15.7% improvement in the total wind field variance explained in the 2004 dataset when IR information is added is comparable to the 17.1% improvement in the developmental dataset. An overall improvement of 15%–17% for the final product is a significant result for this study.

b. Case study of Ivan 2004

To visualize how this algorithm might be put to use in real time, a time series of IR-derived wind fields for Hurricane Ivan is presented in Fig. 10. Ivan was a classic, long-lived Cape Verde hurricane that reached category 5 strength three times on the Saffir–Simpson hurricane scale. Ivan caused considerable damage as it passed through the Caribbean Sea. Figure 10 is a plot of IR-derived and observed wind fields for Hurricane Ivan between 1200 UTC 13 September and 0000 UTC 15 September. At 1200 UTC 13 September, Ivan was at its strongest, exhibiting a minimum sea level pressure of 915 hPa, an observed VMAX of 140 kt, and was passing north through the Yucatan Channel between the Yucatan Peninsula and Cuba. By 0000 UTC 15 September Ivan had weakened slightly to 120 kt, and the winds had become more asymmetric as the storm picked up speed and headed on a more northerly track.

The left-hand panels in Fig. 10 illustrate the IR-derived wind fields, and as is visibly noticeable, they are very close estimations of the actual aircraft-measured wind fields. In fact, at the first and second time periods, the algorithm accurately predicted RMAX within 2 km (actual 34.0 km). It appears as though Ivan was going through an eyewall cycle at 1200 UTC 14 September, and the algorithm could not accurately predict the location of the new outer eyewall. However, by the fourth time period, the algorithm was able to reposition RMAX accurately at 55 km (aircraft-measured RMAX of 54 km). The no-sat version of this algorithm was off on RMAX estimates by at least 10 km at each time period, and was not able to correctly estimate the new outer eyewall at 1200 UTC 14 September. Thus, the IR information appears to be bringing the solution closer to the truth. The algorithm slightly underpredicted V182 (by 2–6 kt) at the first three time periods, but was accurate at 60 kt by the fourth time period. The no-sat method was correct within 4 kt for each time period as well, and as noted before, the IR contribution to V182 estimates is not as important as the contribution to RMAX estimates; however, statistically it is significant when acting on the dataset as a whole. Finally, the addition of a motion vector asymmetry brings the estimation to the final phase. The algorithm accurately portrays the increasingly asymmetric nature of the storm through the 36-h time period, as it sped up. The location, extent, and magnitude of the wind maximum are quite good for each of the four time periods.

6. Summary and conclusions

This study used geostationary IR data to estimate the wind structure of a TC through estimates of RMAX and V182. The estimative algorithms were developed with 405 cases from the 1995–2003 Atlantic and eastern Pacific hurricanes seasons, with a multiple linear regression analysis technique, and independent tests were performed on 50 cases from the 2004 hurricane season. The RMAX and V182 estimates were subsequently used in conjunction with a modified Rankine vortex wind model to estimate the symmetric tangential wind profile out to 202 km from the storm's center. Finally, storm motion derived wind asymmetry was added to

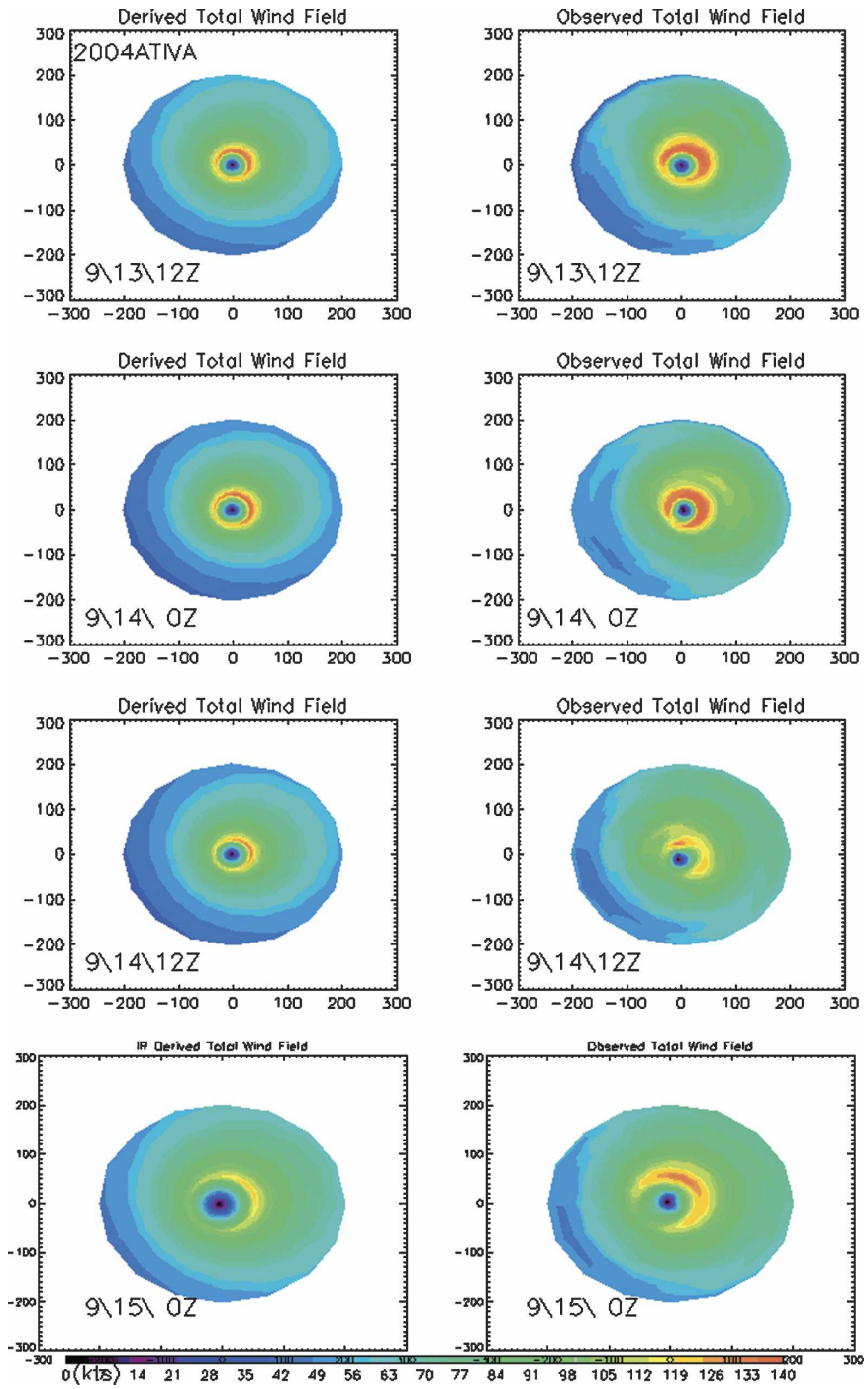

FIG. 10. Plot of (left) IR-derived total wind field and (right) aircraft-measured total wind field for 36 h in the lifetime of Hurricane Ivan in 2004.

the symmetric wind profile to provide a reconstruction of the entire 2D wind field, at each of 51 radial and 16 azimuthal grid points.

In general, because there are no methods prior to this study that provide wind structure estimates from geostationary IR data, the results compared with the no-sat method alone are very promising. In terms of prediction of RMAX, a significantly larger portion of the variance is explained when IR predictors are retained. There are less dramatic, but still significant, improve-

ments in error associated with estimates of V182. Improvements on the order of 16.0% are exhibited for the entire wind field, with 41%–54% of the variance of the total wind field explained by the IR method.

The results of this study suggest that the IR-derived wind field would have application to operational forecasting, especially in regions that do not have routine aircraft data (most of the world except the western Atlantic). In addition, these wind field estimations might also be used to better initialize forecast models in areas where aircraft do not routinely fly (Velden et al. 1992).

Future work includes the extension of the algorithm globally to other tropical basins. Furthermore, the storm motion vector is not capturing the entire asymmetric flow field for each case, especially for those cases that are slow moving. Therefore, it would be interesting to research the relationship between wind asymmetry and other parameters, including convective asymmetries, relative flow field, and wind shear over the domain. By adding other factors into the asymmetric wind analysis, a closer approximation of the actual wind field should be possible. It would be instructive to examine cases where a concentric eyewall is present, and to be able to model these cases using a separate vortex model. Intense tropical cyclones will often have two eyewalls nearly concentric about the center of the storm, the outer eyewall surrounding the inner one. A local wind maximum is generally present in each eyewall. Also, intense systems often undergo eyewall cycles, in which an inner eyewall is replaced by a secondary eyewall at a larger radius. Sometimes more than two eyewalls occur. It will be a challenge to incorporate these effects into a vortex model, and to identify cases in which there is a concentric eyewall structure. Microwave satellite imagery would likely be helpful in this case because it can penetrate the cirrus at the storm top (Hawkins et al. 2001).

A more immediate plan is to combine these analyses with other satellite estimates of the winds around TCs to create an estimate of the flight-level wind field associated with TCs. Such analyses will be of particular use in the majority of the world's TC basins where aircraft reconnaissance is unavailable.

Finally, it should be pointed out that the IR algorithm is estimating flight-level winds, since aircraft observations were used as ground truth. It would be necessary to reduce the winds to the surface for operational forecasting purposes (Franklin et al. 2003; Powell et al. 1998).

Acknowledgments. This research was partially funded by NOAA Grant NA17RJ1228. The authors thank Ray Zehr for the CIRA IR hurricane archive. Views, opinions, and findings in this report are those of the authors and should not be construed as an official NOAA and or U.S. government position, policy, or decision.

REFERENCES

Brueske, K. F., and C. S. Velden, 2003: Satellite-based tropical cyclone intensity estimation using the NOAA-KLM series Advanced Microwave Sounding Unit (AMSU). *Mon. Wea. Rev.,* **131,** 687–697.

DeMaria, M., and R. W. Jones, 1993: Optimization of a hurricane track forecast model with the adjoint model equations. *Mon. Wea. Rev.,* **121,** 1730–1745.

Demuth, J. L., M. DeMaria, J. A. Knaff, and T. H. Vonder Haar, 2004: Evaluation of Advanced Microwave Sounder Unit tropical cyclone intensity and size estimation algorithms. *J. Appl. Meteor.,* **43,** 282–296.

Dunion, J. P., and C. S. Velden, 2002: Application of surface-adjusted GOES low-level cloud-drift winds in the environment of Atlantic tropical cyclones. Part I: Methodology and validation. *Mon. Wea. Rev.,* **130,** 1333–1346.

Dvorak, V. F., 1975: Tropical cyclone intensity analysis and forecasting from satellite imagery. *Mon. Wea. Rev.,* **103,** 420–464.

——, 1984: Tropical cyclone intensity analysis using satellite data. NOAA Tech. Rep. NESDIS 11, 47 pp. [Available from NOAA/NESDIS, 5200 Auth Rd., Washington, DC 20233.]

Franklin, J. L., M. L. Black, and K. Valde, 2003: GPS dropwindsonde wind profiles in hurricanes and their operational implications. *Wea. Forecasting,* **18,** 32–44.

Hawkins, J. D., F. L. Thomas, J. Turk, C. Sampson, J. Kent, and K. Richardson, 2001: Real-time Internet distribution of satellite products for tropical cyclone reconnaissance. *Bull. Amer. Meteor. Soc.,* **82,** 567–578.

Hillger, D. W., and G. P. Ellrod, 2003: Detection of important atmospheric and surface features by employing principal component image transformation of GOES imagery. *J. Appl. Meteor.,* **42,** 611–629.

Holland, G. J., 1980: An analytic model of the wind and pressure profiles in hurricanes. *Mon. Wea. Rev.,* **108,** 1212–1218.

Powell, M. D., S. H. Houston, L. R. Amat, and N. Morisseau-Leroy, 1998: The HRD real-time hurricane wind analysis system. *J. Wind Eng. Ind. Aerodyn.,* **77–78,** 53–64.

Spencer, R. W., and W. D. Braswell, 2001: Atlantic tropical cyclone monitoring with AMSU-A: Estimation of maximum sustained wind speeds. *Mon. Wea. Rev.,* **129,** 1518–1532.

Thacker, W. C., 1988: Fitting models to inadequate data by enforcing spatial and temporal smoothness. *J. Geophys. Res.,* **93,** 10 655–10 665.

Velden, C. S., C. M. Hayden, W. P. Menzel, J. L. Franklin, and J. S. Lynch, 1992: The impact of satellite-derived winds on numerical hurricane track forecasting. *Wea. Forecasting,* **7,** 107–119.

——, T. L. Oleander, and R. M. Zehr, 1998: Development of an objective scheme to estimate tropical cyclone intensity from digital geostationary satellite infrared imagery. *Wea. Forecasting,* **13,** 172–186.

Zehr, R. M., 2000: Tropical cyclone research using large infrared data sets. Preprints, *24th Conf. on Hurricanes and Tropical Meteorology,* Fort Lauderdale, FL, Amer. Meteor. Soc., 486–487.